Results of the SEST key programme: CO in the Magellanic Clouds

VII. 30 Doradus and its southern H II regions[*]

L.E.B. Johansson[1], A. Greve[2], R.S. Booth[1], F. Boulanger[3,4], G. Garay[5], Th. de Graauw[6], F.P. Israel[7], M.L. Kutner[8,9], J. Lequeux[3,10], D.C. Murphy[11], L.–Å. Nyman[12], and M. Rubio[5]

[1] Onsala Space Observatory, S-439 92 Onsala, Sweden
[2] IRAM, 300 rue de la Piscine, Domaine Universitaire, F-38406 St. Martin d'Heres, France
[3] Radioastronomie, Ecole Normale Superieure, 24 rue Lhomond, F-75231 Paris CEDEX 05, France
[4] Institut d'Astrophysique Spatiale, Bat. 120, Université de Paris-XI, F-91045 Orsay CEDEX, France
[5] Departamento de Astronomía, Universidad de Chile, Casilla 36-D, Santiago, Chile
[6] Laboratorium voor Ruimteonderzoek, SRON, Postbus 800, 9700 AV Groningen,The Netherlands
[7] Sterrewacht, Postbus 9513, 2300 RA Leiden, The Netherlands
[8] NRAO, 949 N. Cherry Av., Campus Building 65, Tucson, AZ 85721-0655, USA
[9] Department of Physics, Rensselaer Polytechnic Institute, Troy, NY 12180, USA
[10] DEMIRM, Observatoire de Paris, 61 Av. de l'Observatoire, F-75014 Paris, France
[11] The Observatories of the Carnegie Institution of Washington, 813 Santa Barbara St., Pasadena, CA 91101, USA
[12] European Southern Observatory, Casilla 19001, Santiago 19, Chile

Abstract. We have mapped the ^{12}CO(1–0) emission from the 30 Doradus region in the Large Magellanic Cloud with the Swedish–ESO Submillimetre Telescope (SEST). The regions investigated include the central part of the 30 Dor nebula, and the southern H II regions N 158C, N 159, and N 160. In addition, a few prominent CO clouds have been studied in the (2–1) and (3–2) transitions of CO.

The southern area shows the strongest ^{12}CO(1–0) emission, a factor of 3 higher than towards the central part of 30 Dor. A non–LTE analysis of the CO emission from a sample of clouds indicate kinetic temperatures between 10 and 50 K; the highest temperatures are found close to the 30 Dor nebula. We have estimated the CO–H_2 conversion factor for the two areas, separately, under the assumption that the virial mass, determined from CO parameters, reflects the total molecular mass. We find an unexpectedly small difference between the two areas. This is explained as a bias effect.

Key words: galaxies: individual: LMC – Magellanic Clouds – galaxies: ISM – galaxies: irregular – ISM: molecules – ISM: clouds

1. Introduction

There are only few irregular galaxies and spirals with giant H II regions and luminous stellar clusters as spectacular as 30 Doradus and its southern environment in the Large Magellanic Cloud (LMC). Conspicuous as a large filamentary emission nebula and a chain of bright H II regions speculated to form a small spiral arm at the eastern end of the bar (Laspias & Meaburn 1991, de Vaucouleurs & Freeman 1972), this area contains many objects which manifest past and continuing star formation. Examples are bright stellar clusters of massive young stars (Lucke & Hodge 1970, Hodge 1988a, Parker & Garmany 1993, Hunter et al. 1996, Brandl et al. 1996, Deharveng & Caplan 1991) emitting intense UV radiation (Page & Carruthers 1981, Cheng et al. 1992) and characterized by stellar winds which have created loops and supershells often filled with hot gas emitting X–rays (Elliot et al. 1977, Cox & Deharveng 1983, Chu & Kennicutt 1994, Bomans et al. 1995, Norci & Ögelman 1995), protostellar objects (Jones et al. 1986, Hyland et al. 1992, Heydari–Malayeri & Testor 1986), compact infrared sources (Schwering & Israel 1990, Rubio et al. 1992), OH and H_2O masers (Whiteoak & Gardner 1986, Caswell 1995), supernova remants and a recent supernova explosion, and extended and pointlike X–ray sources of which some may be associated with WR stars (Wang & Helfand 1991, Norci & Ögelman 1995, Wang 1995). The residual material available for current and future star formation in this region is evident as H I and H_2 gas (Rohlfs et al. 1984, Lucks & Rohlfs 1992, Dickey et al. 1994, Israel & Koorneef 1991, Poglitsch et al. 1995), molecular clouds (Co-

hen et al. 1988, Johansson 1991, Israel et al. 1993, Garay et al. 1993), dark nebulae (Hodge 1972, 1988b), and cool dust (Dall'Oglio et al. 1995). Compared with similar or even brighter stellar clusters and H II regions in the irregular galaxies NGC 1705 and NGC 1569, and in M 82 (Hunter 1995), the proximity of the LMC (55 kpc, Westerlund 1990) allows study of the 30 Doradus region and its southern H II regions with high spatial resolution at optical wavelengths or with the SEST at radio wavelengths. Accordingly, detailed knowledge of the various constituents can be obtained rather than simply integrated properties. While the earlier ^{12}CO(1–0) observations of 8$''$8 resolution (equivalent to 140 pc at the LMC) by Cohen et al. (1988) revealed many large molecular–cloud complexes, the SEST resolution of 45$''$at 115 GHz CO(1–0), 23$''$at 230 GHz CO(2–1), and 15$''$at 345 GHz CO(3–2) allows mapping individual molecular clouds at linear scales of about 10, 5, and 3 pc, respectively. This resolution reveals the spatial extent of individual clouds and supports determination of their physical parameters, in particular their velocity dispersions, their CO luminosities, and their masses from application of the virial theorem (MacLaren et al. 1988, Johansson 1991, Garay et al. 1993). Such observations, and the ensemble of deduced physical parameters, may help to quantify the amount of molecular material in metal– and dust–deficient irregulars (Wilson 1995) and to clarify star formation in these galaxies with strong and mostly unshielded UV radiation (Poglitsch et al. 1995, Mochizuki et al. 1994, Israel et al. 1996). This unshielded radiation implies that less molecular material is available for star formation in the LMC than in spiral galaxies. Nevertheless, star formation in irregular galaxies, and in the LMC, may occasionally occur at a rate rarely found in spiral galaxies. Such extreme and perhaps sequential star formation (Walborn & Blades 1997) has occurred in the 30 Doradus region and is progressing towards the south into a large and massive molecular cloud (Israel 1984, Cohen et al. 1988). Surprisingly, even under such extreme conditions, the stars of the young cluster R 136 at the center of 30 Doradus and possibly the stars of the other, not yet investigated, clusters of the southern H II regions, are formed with an IMF which is not significantly different from those of Galactic clusters (Hunter et al. 1996, Brandl et al. 1996).

Here we present a survey of the 30 Doradus region and of the Henize (1956) H II regions N 158C, N 159, and N 160 and their surroundings, made in the ^{12}CO(1–0) transition within the SEST Key Programme. Fig. 1 shows the observed fields and the detected ^{12}CO(1–0) emission overlayed on an SERC blue Schmidt plate. Several areas of these fields were also observed in the (2–1) and (3–2) transitions of ^{12}CO, and in the (1–0) and (2–1) transitions of ^{13}CO. Some results obtained towards the 30 Doradus area have been published earlier by Johansson (1991), Israel et al. (1993; Paper I in the series of SEST Key Programme papers), Booth (1993), Johansson et al. (1994) and Kutner et al. (1997; Paper VI).

Sect. 2 describes the observations and data reduction; Sect. 3 gives the observational results. In Sect. 4 we discuss individual CO clouds and the various cloud parameters derived

from our observations. In the Appendix we explain the derivation of the CO emission parameters presented in Table 1.

2. Observations and data reduction

The ^{12}CO(1–0) observations were made during several 5–7 day observing runs between 1987 and 1994 using the SEST, located on La Silla, Chile. Guided by the results of the ^{12}CO(1–0) survey, observations of higher CO transitions were made towards some prominent CO complexes. The first CO(2–1) observations were made in September, 1987, while CO(3–2) data were taken in February and June, 1992, and in June, 1995. In this paper we also include some results from observations of CS(2–1) and HCO$^+$(1–0), made in June, 1992 and in December, 1995.

In the 100–GHz range a Schottky receiver was used in 1987 – 1994, thereafter we used an SIS mixer. Typical system temperatures T^*_{sys} (corrected for rearward spillover and atmospheric attenuation) were 550 and 300 K, respectively. In the 200–GHz range, the original Schottky receiver ($T^*_{sys} \sim 2000$ K) was replaced by an SIS mixer ($T^*_{sys} \sim 400$ K) in 1990. For the CO(3–2) observations we used an SIS mixer with T^*_{sys} in the range of 300 – 800 K, depending on atmospheric conditions. All receivers were tuned to single–sideband operation.

The backends were acousto–optical spectrometers (AOS) with channel separations of 0.043 MHz (2000 channels) and 0.69 MHz (1440 or 1600 channels). The high-resolution AOS was used in the 100-GHz range while, in general, a low-resolution AOS was used in the higher–frequency bands. The ^{12}CO(1–0) survey was made in frequency–switching mode with a throw of 15 MHz. For the CO(2–1) and (3–2) observations we used almost exclusively dual beam–switching with a throw of about 12$'$ in azimuth. We checked carefully for emission in the reference phase; dubious spectra were re–observed using position switching.

Antenna pointing was checked frequently on the SiO maser R Dor located about 20° from the LMC. Absolute pointing offsets generally did not exceed 10$''$ while relative pointing offsets between adjacent grid positions are less than a few arcseconds.

Two fields were mapped (see Fig. 1), one centered on the 30 Dor nebula, the other on the southern part of the 30 Dor complex, containing the H II regions N 158C, N 159, and N 160. In the following we refer to these fields as the "30 Dor" and the "Southern" areas, respectively. Each field was first mapped with a grid point spacing of 40$''$ (30 Dor) and 60$''$ (Southern). Emission regions detected in this pilot survey were subsequently observed with finer spacings of 20$''$ (30 Dor) and 20$''$ or 30$''$ (Southern). The observed positions are indicated on the channel maps shown in Figs. 2, 3, and 4. The rms noise level in each channel was typically 0.2 K during the pilot survey, and a factor of 2 lower for the more detailed investigations.

The spectra taken in frequency–switching mode suffer from significant baseline curvature. To define the baselines we have tried two methods: i) fitting polynomials to the spectra and ii) using spectra from emission-free regions. The second method was used in most cases, because high–order polynomials were needed to fit the original spectra and these baseline curvatures

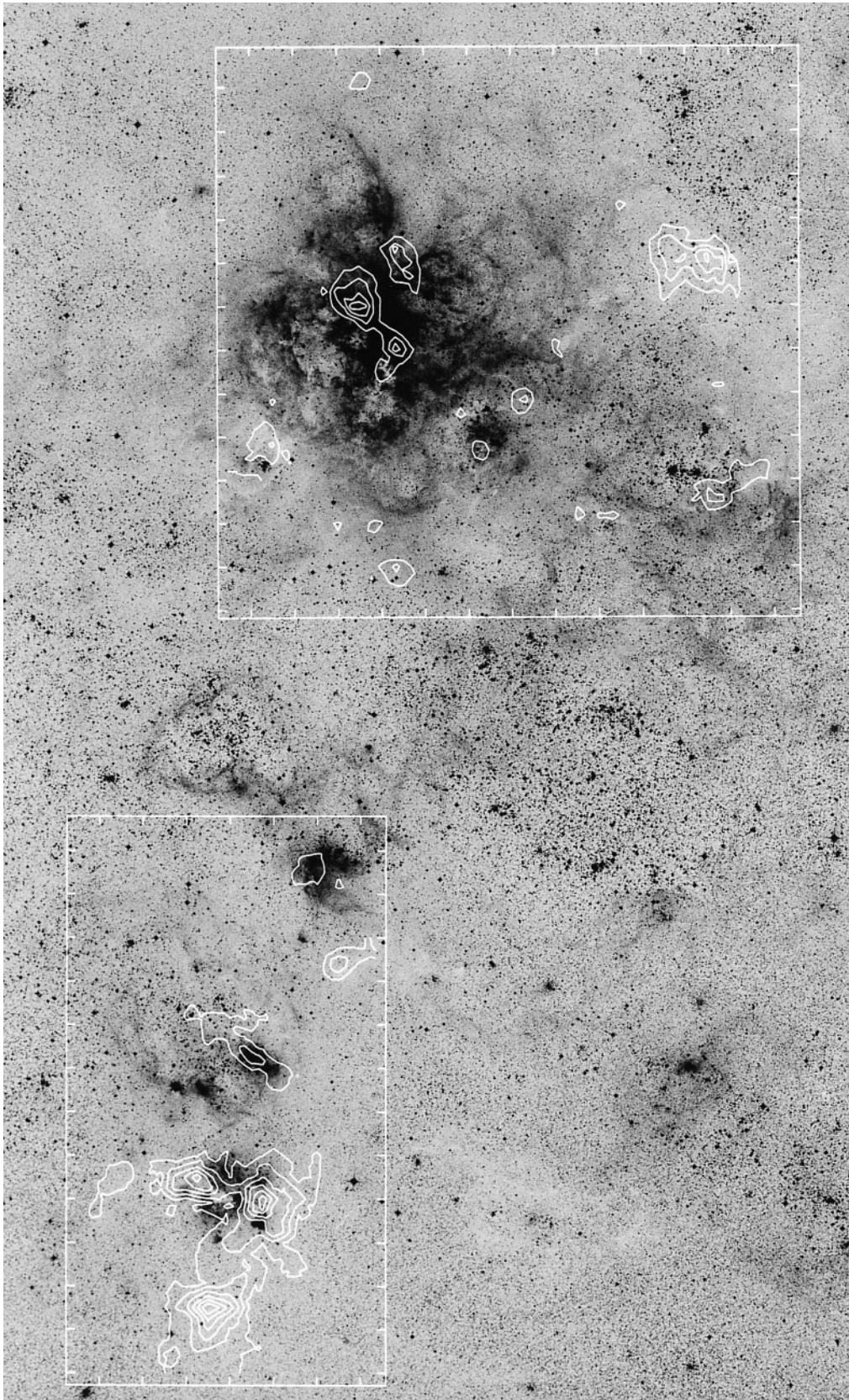**Fig. 1.** Surveyed fields and integrated ^{12}CO(1–0) emission overlayed on an SERC blue Schmidt plate. The northern field contains the 30 Doradus region; the southern field, the H II regions N 158C, N 160, and N 159 (from N to S). North is at the top, East to the left. Tickmarks of 2′ spacings are shown. The fields were not surveyed on a uniform grid; the dots in Figs. 2 and 3 show the observed directions.

Table 1. ^{12}CO(1–0) emission parameters of the surveyed areas

Cloud	$\Delta\alpha$ [a]	$\Delta\delta$ [a]	$\alpha(1950)$	$\delta(1950)$	T_{mb}	V_{lsr}	ΔV	Size	$\log(L_{\mathrm{co}})$	$\log(M_{\mathrm{vir}})$	Em. Neb. [b]
	[']	[']	[h m s]	[° ′ ″]	[K]	[km s^{-1}]	[km s^{-1}]	[pc]	[K km s^{-1} pc^2]	[M$_\odot$]	
30Dor-01	0.8	12.2	05:39:09.5	-68:55:45	1.88	258.0	3.32	4.6	2.991	3.878	
30Dor-02	− 10.9	9.0	05:37:00.0	-68:59:00	0.35	258.1	4.42	–	–	–	
30Dor-03	− 11.1	6.5	05:36:55.5	-69:01:27	0.95	259.7	3.79	< 5	2.701	–	
30Dor-04	− 13.3	5.0	05:36:30.5	-69:02:57	1.04	267.1	6.21	13.5	3.378	4.896	
30Dor-05	3.4	4.8	05:39:38.4	-69:03:14	0.39	256.8	4.52	10.9	2.718	4.528	N 157 A
30Dor-06	− 0.8	4.3	05:38:50.7	-69:03:39	2.18	249.4	4.48	13.4	3.551	4.610	N 157 A
30Dor-07	− 13.2	4.2	05:36:32.0	-69:03:47	1.12	273.9	6.66	16.9	3.564	5.054	
30Dor-08	− 15.0	4.0	05:36:11.9	-69:04:01	2.33	259.8	5.90	20.9	3.967	5.041	
30Dor-09	− 9.8	2.3	05:37:10.3	-69:05:43	0.36	276.9	4.58	7.8	2.551	4.390	
30Dor-10	1.0	2.2	05:39:11.2	-69:05:47	1.38	248.7	11.23	20.1	3.994	5.583	N 157 A
30Dor-11	− 9.8	0.1	05:37:28.9	-69:07:52	1.23	252.8	3.27	2.4	2.792	3.596	N 157 A
30Dor-12	− 0.6	0.1	05:38:52.9	-69:07:54	2.60	246.5	3.01	< 5	3.035	–	N 157 A
30Dor-13	− 1.0	0.0	05:38:49.2	-69:07:58	2.79	249.8	2.26	4.5	3.035	3.541	
30Dor-14	4.3	0.0	05:39:50.0	-69:08:00	0.40	270.2	2.41	–	–	–	
30Dor-15	0.0	− 1.0	05:38:59.6	-69:09:00	1.40	246.2	3.39	10.4	3.120	4.255	N 157 A
30Dor-16	3.3	− 1.0	05:39:37.3	-69:09:02	0.96	266.8	3.10	10.0	2.904	4.163	N 157 A
30Dor-17	− 6.5	− 2.3	05:37:47.4	-69:10:21	2.09	248.0	3.76	7.0	3.209	4.173	N 157 B
30Dor-18	− 3.9	− 2.9	05:38:16.4	-69:10:57	0.89	247.3	3.24	10.0	2.885	4.198	N 157 B
30Dor-19	3.2	− 3.3	05:39:36.1	-69:11:18	0.50	283.8	4.58	5.6	2.625	4.251	N 157 A
30Dor-20	5.4	− 4.3	05:40:01.4	-69:12:17	1.02	277.1	5.65	17.5	3.466	4.927	
30Dor-21	5.0	− 4.3	05:39:56.0	-69:12:20	0.41	257.5	8.10	–	–	–	
30Dor-22	− 4.6	− 4.6	05:38:08.7	-69:12:36	1.00	249.3	4.53	6.8	2.962	4.323	N 157 B
30Dor-23	− 6.0	− 6.0	05:37:53.2	-69:13:58	0.60	254.7	3.54	4.6	2.564	3.935	
30Dor-24	− 6.9	− 6.5	05:37:42.9	-69:14:29	1.01	255.9	2.79	4.8	2.694	3.751	
30Dor-25	− 15.7	− 3.3	05:36:04.0	-69:11:20	0.54	269.0	3.39	–	–	–	
30Dor-26	− 16.7	− 5.7	05:35:53.0	-69:13:40	0.49	253.5	13.20	–	–	–	
30Dor-27	− 15.1	− 6.5	05:36:10.4	-69:14:31	2.13	240.0	3.95	10.4	3.366	4.386	
30Dor-28	− 15.7	− 6.7	05:36:04.0	-69:14:40	0.56	257.0	8.10	–	–	–	
30Dor-29	− 9.3	− 7.3	05:37:15.6	-69:15:16	0.95	247.1	4.25	12.4	3.126	4.530	
30Dor-30	− 10.7	− 7.7	05:36:59.7	-69:15:42	0.83	246.6	4.17	6.5	2.837	4.231	
30Dor-31	0.3	− 8.1	05:39:03.8	-69:16:06	1.09	249.6	2.64	5.7	2.732	3.780	
30Dor-32	1.6	− 9.2	05:39:17.8	-69:17:10	0.64	249.0	3.64	9.0	2.761	4.257	
30Dor-33	− 0.6	− 10.3	05:38:53.6	-69:18:16	1.41	250.6	3.49	11.0	3.160	4.308	
N158-1	− 4.0	15.6	05:39:31.9	-69:31:21	3.78	257.7	3.48	10.5	3.538	4.283	N 158 C
N158-2	− 3.2	14.8	05:39:40.6	-69:32:10	1.45	250.8	2.74	9.9	3.024	4.050	N 158 C
N158-3	− 5.0	14.4	05:39:20.3	-69:32:35	1.62	254.7	3.88	6.2	3.086	4.152	N 158 C
N158-4	− 5.2	11.0	05:39:17.6	-69:36:01	1.66	247.6	5.79	13.4	3.539	4.831	
N158-5	− 4.9	10.7	05:39:21.7	-69:36:18	2.05	252.7	5.98	9.9	3.515	4.730	
N160-1	0.7	8.0	05:40:26.9	-69:38:59	2.70	233.7	2.68	6.8	3.169	3.870	N 160 AD
N160-2	0.2	8.0	05:40:20.3	-69:39:02	2.90	229.1	3.04	12.3	3.463	4.232	N 160 AD
N160-3	1.1	7.3	05:40:30.5	-69:39:43	0.55	225.5	3.81	6.1	2.913	4.126	N 160 AD
N160-4	− 1.0	6.5	05:40:06.2	-69:40:29	3.29	237.0	4.66	10.3	3.625	4.528	N 160 AD
N160-5	− 2.1	5.6	05:39:53.7	-69:41:24	1.62	241.5	5.78	11.5	3.459	4.764	N 160 AD
N160-6	5.1	1.0	05:41:17.4	-69:46:01	2.94	231.4	3.70	11.3	3.517	4.370	
N159-E	1.5	0.8	05:40:35.2	-69:46:13	5.24	234.1	7.62	19.2	4.373	5.226	N 159 BGC
N159-W	− 1.4	0.1	05:40:02.0	-69:46:53	6.58	238.5	5.97	16.7	4.277	4.953	N 159 JFID
N159-1	6.1	− 0.5	05:41:29.4	-69:47:33	1.63	233.1	4.27	6.8	3.152	4.274	
N159-2	− 2.0	− 1.3	05:39:55.0	-69:48:17	4.86	233.6	5.48	14.8	4.041	4.828	N 159 A
N159-S	0.7	− 4.9	05:40:26.5	-69:51:56	5.81	234.6	8.48	21.8	4.550	5.374	
N159-3	1.2	− 6.1	05:40:32.5	-69:53:06	2.69	231.4	6.96	17.1	3.973	5.098	

a) Offsets are relative to 05^{h}39^{m}00^s.2, −69°08′00″ and 05^{h}40^{m}18^s.2, −69°47′00″ (1950.0) for sources in the 30 Doradus region and the Southern field of H II regions, respectively. b) Coincidence with Henize (1956) emission nebulae.
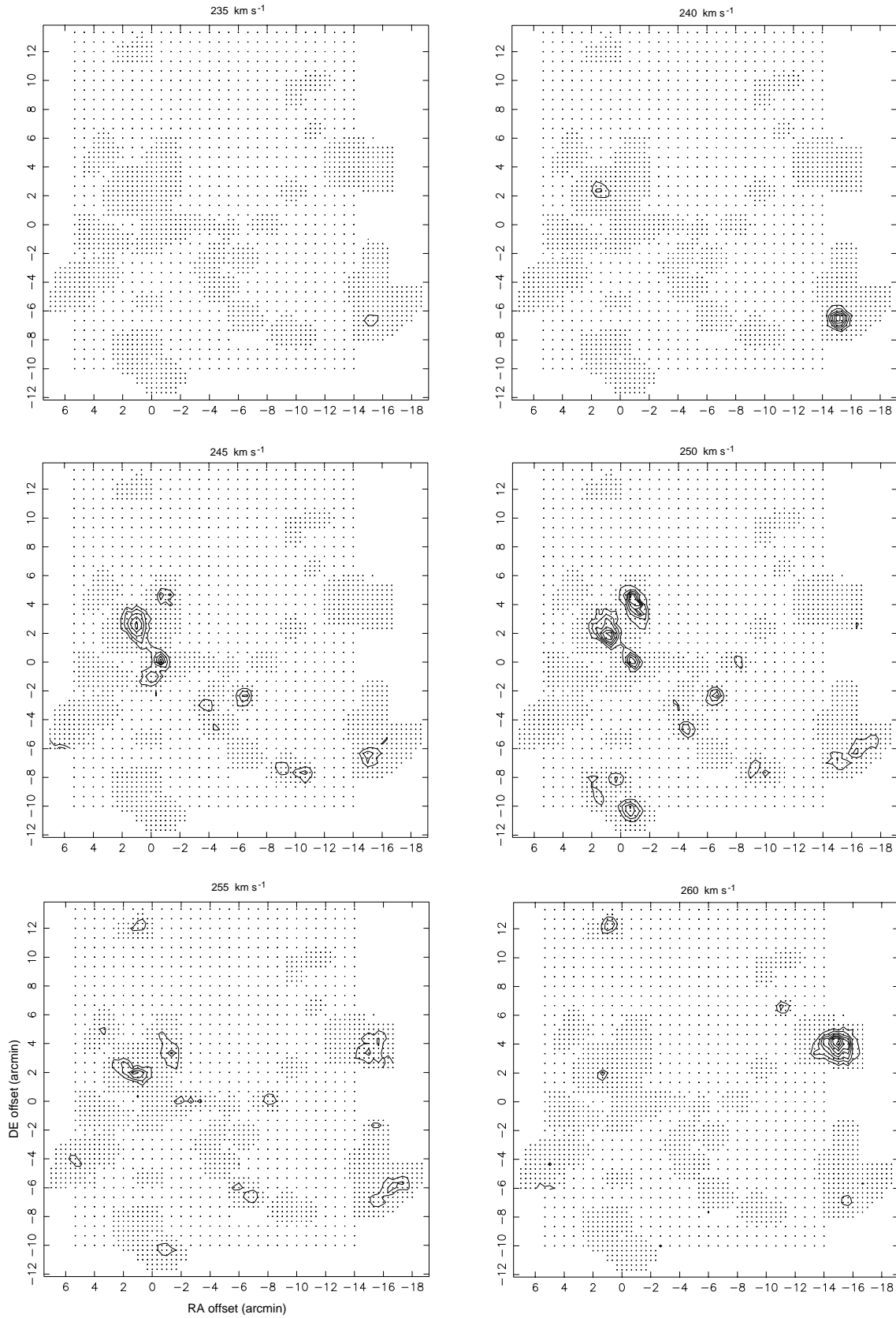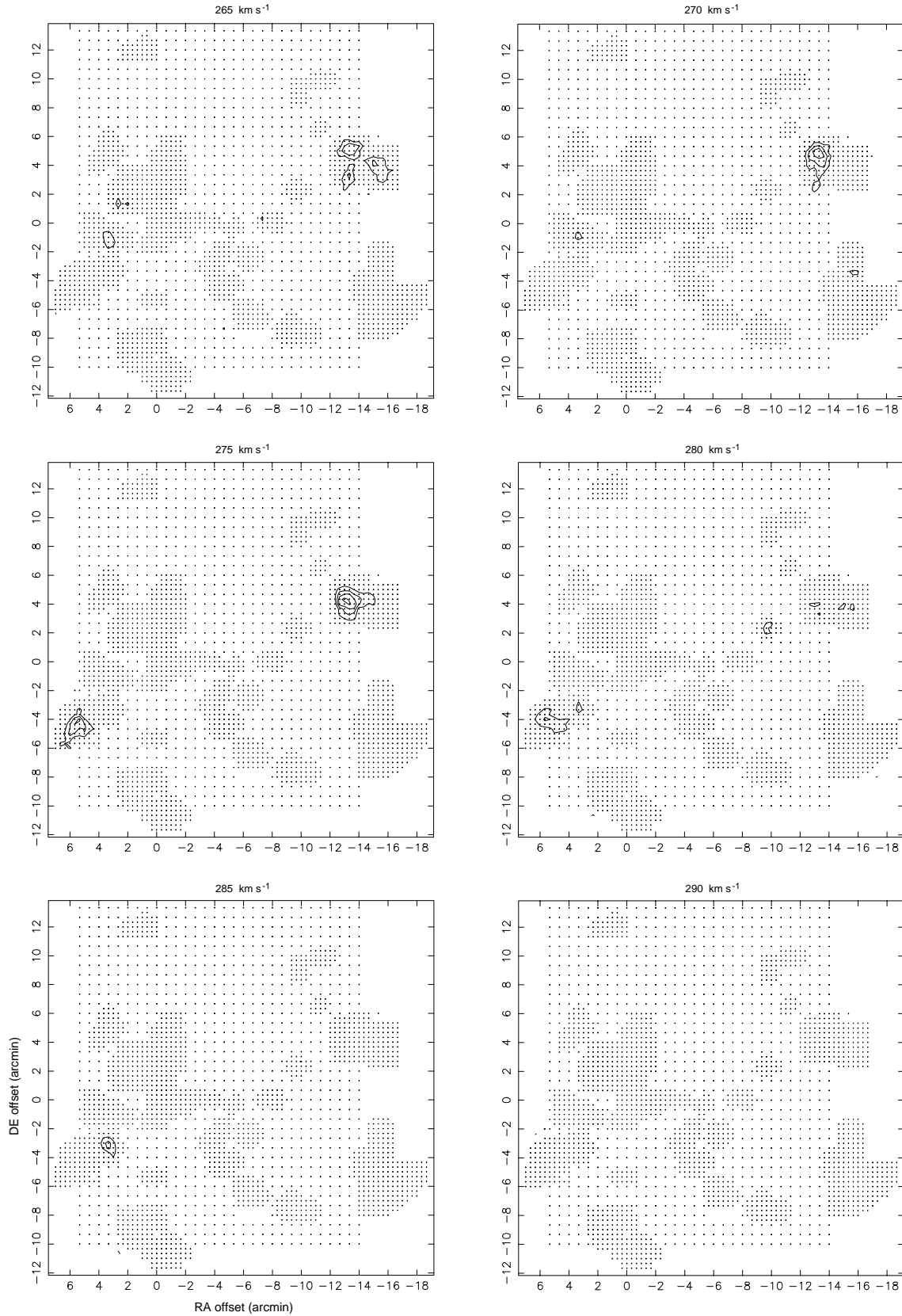Lack of entry in the column "Size" indicates that the emission is complex or weak.

Fig. 2. Contour maps in the 30 Doradus area of the ^{12}CO(1–0) emission integrated over velocity intervals of 5 km s^{-1} width, centered as indicated. The contour levels are 1 to 11 by 1 K km s^{-1} in the T_A^* scale. Observed positions are indicated by dots. The center of the field is at $05^h39^m00^s2$ and $-69°08'00''$ (1950.0).

Fig. 3. Contour maps in the 30 Doradus area of the ^{12}CO(1–0) emission integrated over velocity intervals of 5 km s^{-1} width, centered as indicated. The contour levels are 1 to 11 by 1 K km s^{-1} in the T_A^* scale. Observed positions are indicated by dots. The center of the field is at 05^{h}39^{m}00^{s}2 and $-69°08'00''$ (1950.0).
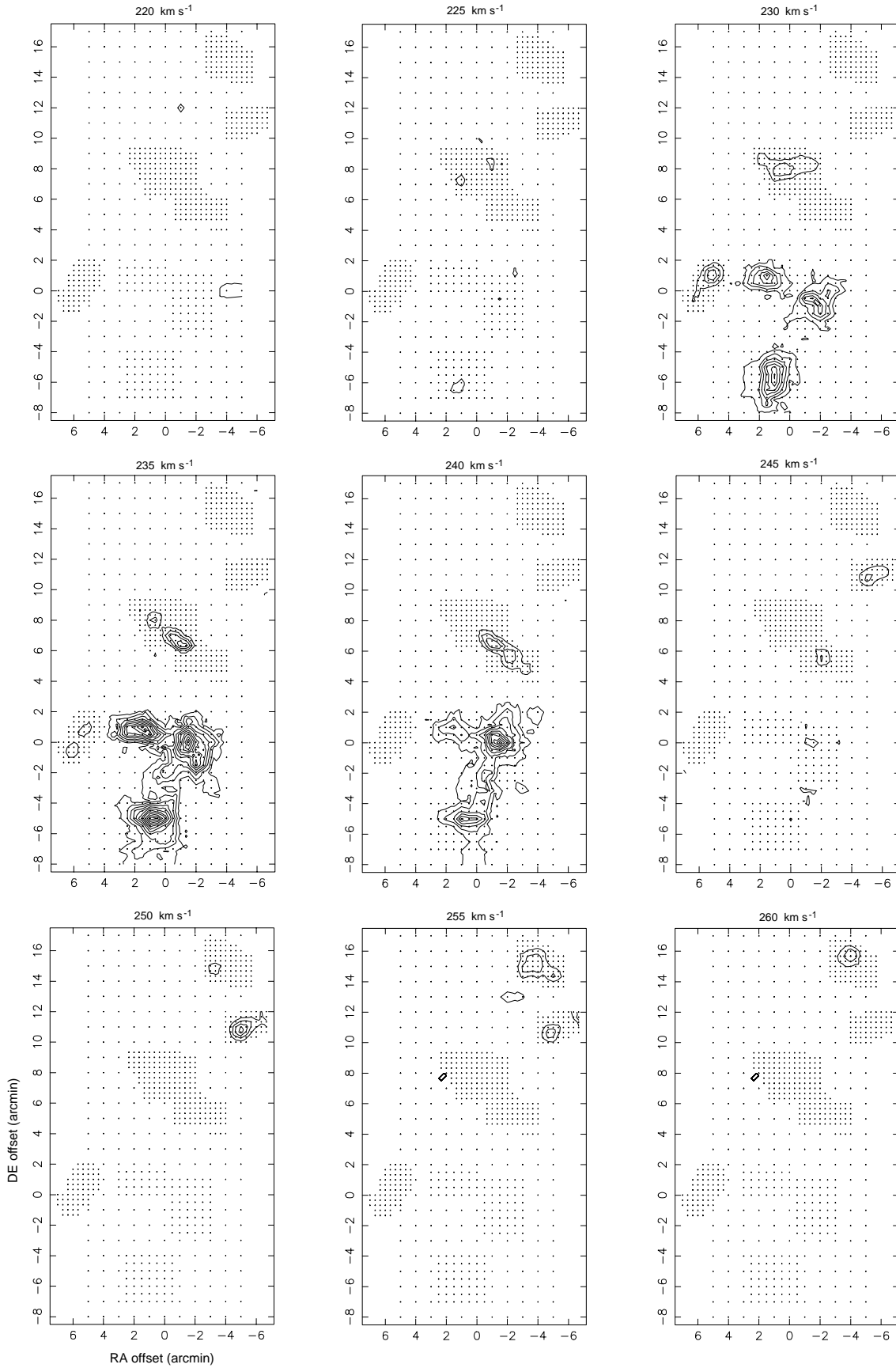
Fig. 4. Contour maps in the Southern field, containing the H II regions H 158C, N 160, N 159 (from N to S), of the ^{12}CO(1–0) emission integrated over velocity intervals of 5 km s^{-1} width, centered as indicated. The contour levels are 2 to 22 by 2 K km s^{-1} in the T_A^* scale. Observed positions are indicated by dots. The center of the field is at $05^h40^m18^s2$ and $-69°47'00''$ (1950.0).

Table 2. CO cloud sizes

Cloud	Transition	$\Delta\alpha$ [a] ["]	$\Delta\delta$ [a] ["]	V_{lsr} [km s^{-1}]	ΔV [km s^{-1}]	Size [pc]
30Dor-01	^{12}CO(1–0)	50	735	258.0	3.3	5
	^{12}CO(2–1)	57	741	258.1	5.1	9
	^{12}CO(3–2)	43	732	257.9	2.6	7
30Dor-06	^{12}CO(1–0)	–51	261	249.4	4.5	13
	^{12}CO(2–1)	–41	261	249.8	5.7	10
30Dor-08	^{12}CO(1–0)	–899	239	259.8	5.9	21
	^{12}CO(2–1)	–890	240	260.2	6.3	16
30Dor-10	^{12}CO(1–0)	59	133	248.7	11.2	20
	^{12}CO(2–1)	51	126	249.6	10.9	12
	^{12}CO(3–2)	54	125	249.3	9.6	10
30Dor-17	^{12}CO(1–0)	–389	–141	248.0	3.8	7
	^{12}CO(2–1)	–388	–144	248.0	5.5	7
	^{12}CO(3–2)	–381	–134	247.8	4.2	9
30Dor-27	^{12}CO(1–0)	–907	–391	240.0	4.0	10
	^{12}CO(2–1)	–906	–397	239.9	4.8	9
	^{12}CO(3–2)	–905	–386	239.7	4.8	11
30Dor-33	^{12}CO(1–0)	–35	–616	250.6	3.5	11
	^{12}CO(2–1)	–37	–615	251.4	3.3	8
N159-W	^{12}CO(1–0)	–84	7	238.5	6.0	17
	^{12}CO(2–1)	–78	4	237.7	8.0	13
	^{12}CO(3–2)	–84	9	238.0	6.7	17
	^{13}CO(2–1)	–89	6	238.4	5.4	9

a) Offsets are relative to $05^h39^m00\overset{s}{.}2$, $-69°08'00''$ and $05^h40^m18\overset{s}{.}2$, $-69°47'00''$ (1950.0) for sources in the 30 Dor region and in the Southern field of H II regions, respectively.

turned out to be relatively stable over time scales of hours. "Emission-free" regions were selected in the data–reduction process. Spectra from these regions were added and smoothed to a high degree, and then subtracted from the original data. After folding, a simple cleaning process was used to remove the reference features which result from the frequency–switching method. Starting with the strongest emission in a spectrum, a Gaussian fit was used to remove the reference features at velocities defined by the frequency throw. This was repeated for successively weaker lines, down to the detection limit. It should be emphasized that this definition of baselines will leave extended and low–level emission undetected. This is also the case with the polynomial method, which, in addition, can mask localized and broad features. However, we have the impression that both methods give very similar results.

The FWHM beams of the SEST are 45″, 23″, and 15″ at 115, 230, and 345 GHz, respectively. The nominal main–beam efficiencies were 0.72, 0.57, and 0.27 at these frequencies. While the antenna gain is essentially constant in the 100–GHz range, the gain changes significantly with elevation in the 200–GHz

and 300–GHz bands. In addition, the relative importance of the error beam may increase at low elevations. However, the CO complexes investigated in the higher transitions are extended relative to the size of the main beam, thus reducing the variations in the beam–source coupling with elevation. This has been verified by observations of the ^{12}CO(3–2) transition, i.e. we observed no noticable changes of the integrated intensities of a $1'$ source in an elevation range where the gain–elevation curve predicts differences by a factor of 2.

Lacking detailed knowledge of the antenna response at the higher frequencies, we estimated the beam–source coupling by introducing the contribution from the error beam. Our analysis of the SEST reflector measurements (N.D. Whyborn & D. Morris, priv. comm.) gives a correlation length for the surface errors of 0.9 m. This is close to the panel size of the reflector and translates to error–beam sizes (Baars 1973, Rohlfs 1990) of $3'$ and $2'$ at 230 GHz and 345 GHz, respectively. To estimate the amplitude of the error beam, we assume that the difference between the moon–beam and main–beam efficiencies is due to the contribution of the error beam. Using the typical extents of CO emission in the LMC, we arrive at beam efficiencies of 0.60 and 0.30 – 0.35 at 230 GHz and 345 GHz, respectively. These numbers refer to elevations where the gain–elevation curves peak $(60° - 70°)$ while the high transition data of CO were taken in the range $42° - 50°$. However, in accordance with the CO(3–2) observations (see above), we assume a negligible elevation dependence for extended sources and compensate by assigning large errors. We use 0.72, $0.60 \pm 20\%$, and $0.33 \pm 30\%$ for the main–beam efficiencies at 115, 230, and 345 GHz, respectively. The errors indicated apply to intensities observed at 230 and 345 GHz relative those at 115 GHz. These numbers have been used in the radiative–transfer analysis of the CO emission (see Sect. 4) where the results are defined by intensity ratios rather than by absolute intensities. With respect to an absolute–intensity scale, we estimate that the error in the main–beam efficiency at 100 GHz is less than $\pm 10\%$. To convert from (on–line) temperatures T_A^* ("chopper" calibrated) to main–beam brightness temperatures, T_{mb}, we use the relation $T_{mb} = T_A^*/\eta(mb)$, where $\eta(mb)$ refers to the main–beam efficiencies above.

3. Results

For the 30 Dor area and the Southern field Figs. 2, 3, and 4 show the contour maps of the integrated ^{12}CO(1–0) emission $I(CO) = \int T_A^* dv$, for velocity intervals of 5 km s^{-1}. Peak antenna temperatures are typically a factor of 3 higher in the Southern field. As pointed out in Sect. 4, this is more likely the effect of different CO filling factors than of different excitation conditions.

The contour maps show well-defined regions of localized CO emission, surrounded by large areas with CO intensities below the detection limit. In Table 1 we list discernible ^{12}CO peaks and some basic properties of the emission. With a few exceptions, Table 1 gives the results of Gaussian fits, in velocity and on the sky (see the Appendix), to the observed spectra at positions surrounding the peaks. This procedure has only been

applied to regions mapped with a grid spacing of $30''$ or smaller. The remaining entries refer to data obtained for single positions (labelled 30Dor-02, 14, 21, 25, 26, and 28).

Columns 2 and 3 of Table 1 give the offsets (arcmin) of the CO peaks relative to the center positions of the fields. Columns 4 and 5 list the resulting equatorial coordinates for the epoch 1950.0. The results of the Gaussian fits are given in Columns 6 to 8, i.e. main–beam brightness temperature, velocity in the lsr system, and line width (full width at half maximum), respectively. Column 9 gives CO sizes (full width at half maximum), corrected for beam smearing. The corresponding CO luminosities and virial masses are listed in Columns 10 and 11, respectively. The uncertainties in the intensities are typically 10 to 20%, while velocities and line widths suffer from errors between 0.1 and 0.5 km s^{-1}. The larger errors apply to weak signals and/or regions of complex emission.

In Figs. 5 and 6 we show the ^{12}CO(3–2) spectra obtained towards the central part of the 30 Dor nebula and the H II region N 159. Both maps show a number of velocity components of which the dominant components are also visible in the ^{12}CO(1–0) and (2–1) data. To trace possible deviations in the spatial distribution of the emission in the three CO transitions, we performed a similar analysis of the higher-transition data as was done for for the ^{12}CO(1–0) data. The results for the most prominent velocity components in some areas are presented in Table 2. Less significant components are not listed, but have been taken into consideration in the Gaussian analysis. Columns 2 and 3 of Table 2 give the offsets, relative to the field centers, for the different CO transitions. For all regions the peak positions agree within the errors defined by the telescope pointing and the Gaussian fits. The velocities (Column 5) and line widths (Column 6) show deviations larger than the formal observational errors; however, they are still within the errors of the Gaussian decomposition of the velocity components. The same applies to the beam–corrected CO sizes (Column 7).

4. Discussion

4.1. CO cloud properties

As indicated in the previous sections, the bulk of the CO emission originates in clouds or cloud complexes with sizes no larger than approximately 20 pc (see Table 1); this upper limit applies to both fields. However, the ^{12}CO(1–0) intensities are significantly higher in the Southern field than in the 30 Dor area, by a factor of 3 in terms of peak antenna temperatures and a factor of 5 when integrated over the maps. This indicates a succesively larger difference between the two areas in CO filling factors with increasing size scales. It is thus conceivable that the CO filling factor also plays an important role on scales smaller than the beam size.

To explore the physical properties of the molecular gas in the LMC, we performed a non–LTE analysis of the CO emission for a sample of clouds residing in different environments. The model treats the radiative transfer by mean escape probabilities (MEP) with coupled equations of statistical equilibrium

for the collisional and radiative rates (see van Dishoeck et al. 1991, Jansen 1995). The clouds are assumed to be isothermal and spherical with constant density and constant CO abundance. Obviously, these latter constraints are physically unrealistic, implying uniform excitation on a 10–pc scale (the beam size in the 100–GHz band). However, here we focus on differences within the sample, possibly correlated with other tracers of the physical properties of the gas, rather than on quantitative results. The underlying assumption is that the errors caused by these constraints are similar for the whole sample.

Table 3 presents the input data and the solutions for 7 clouds in the 30 Dor area and for one cloud associated with the H II region N 159. The latter source is the same cloud investigated by Johansson et al. (1994) in a number of molecular transitions. Columns 3 to 6 of Table 3 give $T_{\rm mb}$, the center velocity, line width, and I(CO), respectively, of the CO transitions indicated in Column 2. All intensities refer to the ^{12}CO(1–0) beam size ($45''$); the higher–transition data have been convolved using the algorithm described by Johansson et al. (1994). The range of the solutions is subject to the following conditions: i) the errors of the ratios $I(CO(2-1))/I(CO(1-0))$ and $I(CO(3-2))/I(CO(1-0))$ are $\pm$ 20% and $\pm$ 30%, respectively (the same errors apply to the two CO isotopomers considered), and ii) the lower limits of the ^{12}CO(1–0) and ^{13}CO(1–0) brightness temperatures are the deconvolved $T_{\rm mb}$ assuming ^{12}CO(1–0) emission extents given in Table 1. We investigated the full parameter space, but in Table 3 we present only the solutions for a fixed H$_2$ density of $\log(n(H_2)) = 4.5$, a density for which all clouds in the sample have solutions. Lower limits of $\log(n(H_2))$ are, in general, 3.5 – 4, while the upper limits are close to 5, or undefined. It should be emphasized that the general results, discussed below, are independent of whether the full parameter space, or the results presented in Table 3, are considered. The solutions, given in Column 7, are the kinetic temperature, the total column density of ^{12}CO, and the surface filling factor of the ^{12}CO emission within the ^{12}CO boundary. This definition implies that the filling factor is independent of the CO cloud size, and thus characterizes the internal structure of the clouds.

The solutions indicate that three clouds (30Dor 6, 10, 17) are warmer than the rest of the sample; these clouds are located in the immediate neighbourhood of the star cluster R 136 with associated photon–dominated region (hereafter PDR). The same clouds also seem to exhibit a lower filling factor of the CO emission, indicating that the gas is highly clumped. This is in line with early attempts to explain the weak CO emission observed in the Magellanic Clouds (see e.g. Israel et al. 1986, Elmegreen 1989) and, later, with arguments or modelling based on improved CO data (Garay et al. 1993, Lequeux et al. 1994). Further support for clumping of the CO gas is provided by the more recent observations of the [CII] emission in the LMC (Mochizuki et al. 1994, Poglitsch et al. 1995, Israel et al. 1996), showing significantly higher PDR-to-molecular-mass ratios (as indicated by the [CII]/CO emission ratios) than in the Galaxy. However, the [CII]/CO ratios show a range of three orders of magnitude from cloud to cloud within the LMC (Israel et al. 1996). In Table 3,

Table 3. Results of a non–LTE analysis of the CO emission from a sample of clouds (see text)

Cloud	Transition	T_{mb} [K]	V_{lsr} [km s^{-1}]	ΔV [km s^{-1}]	I_{co} [K km s^{-1}]	Model results [a] $[n(H_2)=10^{4.5}]$	CS/CO	HCO$^+$/CO	[CII]/CO
30Dor-01	^{12}CO(1-0)	1.7	258.5	3.7	6.5	$T_{kin} = 10 - 13$ K	1.5	0.5	
	^{12}CO(2-1)	1.2	258.1	5.2	6.7	log $N_{co} > 16.0$			
	^{12}CO(3-2)	1.6	258.3	3.1	5.3	filling = $1.0 - 0.7$			
	^{13}CO(1-0)	0.20	258.4	3.2	0.71				
	^{13}CO(2-1)	0.23	258.4	3.5	0.90				
30Dor-06	^{12}CO(1-0)	2.3	249.9	3.8	9.5	$T_{kin} > 20$ K	1.2	1.6	
	^{12}CO(2-1)	1.9	249.1	5.9	12.	log $N_{co} = 16.5 - 17.4$			
	^{12}CO(3-2)	2.9	249.9	5.3	16.	filling < 0.6			
	^{13}CO(1-0)	0.13	249.8	3.2	0.45				
30Dor-08	^{12}CO(1-0)	2.7	260.2	5.3	15.	$T_{kin} = 8 - 11$ K	<0.6	0.3	
	^{12}CO(2-1)	1.4	260.2	6.4	9.8	log $N_{co} > 16.4$			
	^{13}CO(1-0)	0.25	260.4	4.4	1.1	filling = $1.0 - 0.5$			
30Dor-10	^{12}CO(1-0)	1.5	249.7	8.3	13.	$T_{kin} = 40 - 80$ K	2.0	3.4	20
	^{12}CO(2-1)	1.6	250.7	8.8	15.	log $N_{co} = 16.9 - 17.1$			
	^{12}CO(3-2)	2.6	249.9	9.6	27.	filling = $0.1 - 0.05$			
	^{13}CO(1-0)	0.13	249.6	6.3	0.90				
	^{13}CO(2-1)	0.27	250.0	8.0	2.3				
30Dor-17	^{12}CO(1-0)	2.2	248.0	3.7	8.6	$T_{kin} = 20 - 30$ K	1.2	1.2	
	^{12}CO(2-1)	1.7	248.1	5.5	9.8	log $N_{co} = 16.0 - 16.4$			
	^{12}CO(3-2)	2.2	247.7	5.2	12.	filling = $1.0 - 0.3$			
	^{13}CO(1-0)	0.20	248.0	3.7	0.82				
	^{13}CO(2-1)	0.43	247.7	3.3	1.5				
30Dor-27	^{12}CO(1-0)	2.3	239.8	3.8	9.1	$T_{kin} = 11 - 15$ K	1.5	0.5	
	^{12}CO(2-1)	1.4	240.0	4.9	7.5	log $N_{co} = 16.1 - 16.3$			
	^{12}CO(3-2)	1.9	239.5	4.3	8.8	filling = $1.0 - 0.7$			
	^{13}CO(1-0)	0.24	239.4	3.4	0.82				
	^{13}CO(2-1)	0.27	239.6	3.5	1.0				
30Dor-33	^{12}CO(1-0)	1.5	250.8	3.4	5.5	$T_{kin} > 8$ K	<1.0	<0.4	
	^{12}CO(2-1)	0.95	251.4	5.4	5.5	log $N_{co} > 15.8$			
	^{13}CO(1-0)	0.19	251.4	3.1	0.66	filling < 1.0			
N159-W	^{12}CO(1-0)	6.9	237.8	7.5	56.	$T_{kin} = 16 - 23$ K	1	1	1
	^{12}CO(2-1)	6.3	237.6	8.2	52.	log $N_{co} = 17.0 - 17.4$			
	^{12}CO(3-2)	7.3	237.4	8.3	64.	filling = $1.0 - 0.7$			
	^{13}CO(1-0)	0.80	237.6	7.8	6.8				
	^{13}CO(2-1)	1.4	237.4	7.4	11.				
N159-E	^{12}CO(1-0)	5.1	234.2	6.8	37.		0.7	0.9	2
	^{13}CO(1-0)	0.44	234.1	6.6	3.1				
N159-S	^{12}CO(1-0)	6.1	235.4	7.5	49.		0.6	0.2	0.1
	^{13}CO(1-0)	0.72	235.5	5.9	4.5				

a) "filling" refers to surface filling factor

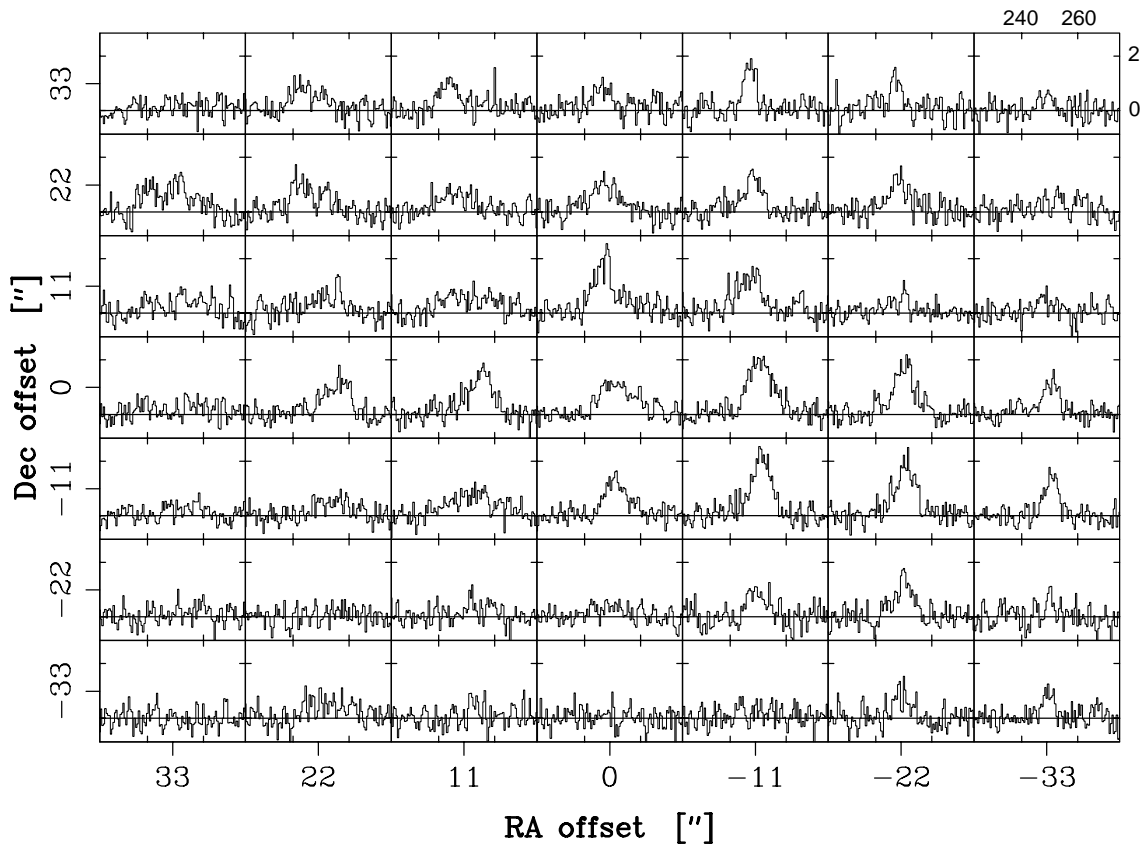**Fig. 5.** ^{12}CO(3–2) spectra observed in the central part of 30 Doradus (30Dor-10). Offsets are relative to $05^h39^m11^s.4$, $-69°06'00''$ (1950.0). The intensity scale is T_A^* [K] and velocities are given relative to lsr [km s^{-1}]. The velocity resolution is 0.5 km s^{-1}. The intensity and velocity scales are indicated in the upper righthand panel.

we have, where available, included these ratios for the clouds in our sample. For comparison, we also list our CS(2–1)/CO(1–0) and HCO$^+$(1–0)/CO(1–0) emission ratios. All ratios are normalized to those observed in cloud N159-W: 0.03, 0.08, and 0.28 (the latter is a luminosity ratio, see Israel et al. 1996) for CS/CO, HCO$^+$/CO, and [CII]/CO, respectively.

The HCO$^+$/CO and [CII]/CO ratios show the same trend, indicating that also the former ratio traces PDRs. All ratios are qualitatively consistent with model predictions of the chemistry in dense PDRs (Sternberg & Dalgarno 1995). While the abundances of CS as well as HCO$^+$ peak in the core region, HCO$^+$ is also abundant in the outer layers where C$^+$ abundances are high. In dark cores, the formation of HCO$^+$ is dominated by a reaction between H$_3^+$ and CO, while in less dense regions C$^+$ is a major component in the formation path of HCO$^+$ (Graedel et al. 1982). Provided that the latter path is significant, one would expect the HCO$^+$ emission to follow that of C$^+$ and to be more extended than that of CS and other high-density tracers towards PDRs. The latter property is observed in the N159-W cloud (Johansson et al. 1994). In contrast, the CS/CO emission ratios are rather constant with no obvious correlation with cloud properties, a

result in agreement with the model by Sternberg & Dalgarno (1995).

4.2. The CO–to–H_2 conversion factor

Several attempts have been made to determine the CO – H$_2$ conversion factors of the Magellanic Clouds (Cohen et al. 1988, Johansson 1991, Israel & de Graauw 1991, Rubio et al. 1993, Garay et al. 1993, Wilson 1995, Chin et al. 1997). Based on SEST observations, the estimates range from close to the canonical value for the Galaxy, 2.3 10^{20} cm^{-2} (K km s^{-1})$^{-1}$ (Strong et al. 1988), to a factor of a few higher. These results assume that the virial mass is a measure of the H$_2$ mass, an assumption questioned by several authors (e.g. Issa et al. 1990, Maloney 1990). However, Maloney also points out that the conversion factors derived from the virial theorem and γ–rays agree well for clouds with masses greater than about 10^5 M$_\odot$. Recently, Rubio (1997) compiled conversion factors based on the virial theorem for clouds in the Galaxy and in the Magellanic Clouds. The analysis indicates that clouds in the inner Galaxy have conversion factors similar to the value determined from γ–rays (Strong et al. 1988), while the average value for clouds in the outer parts is
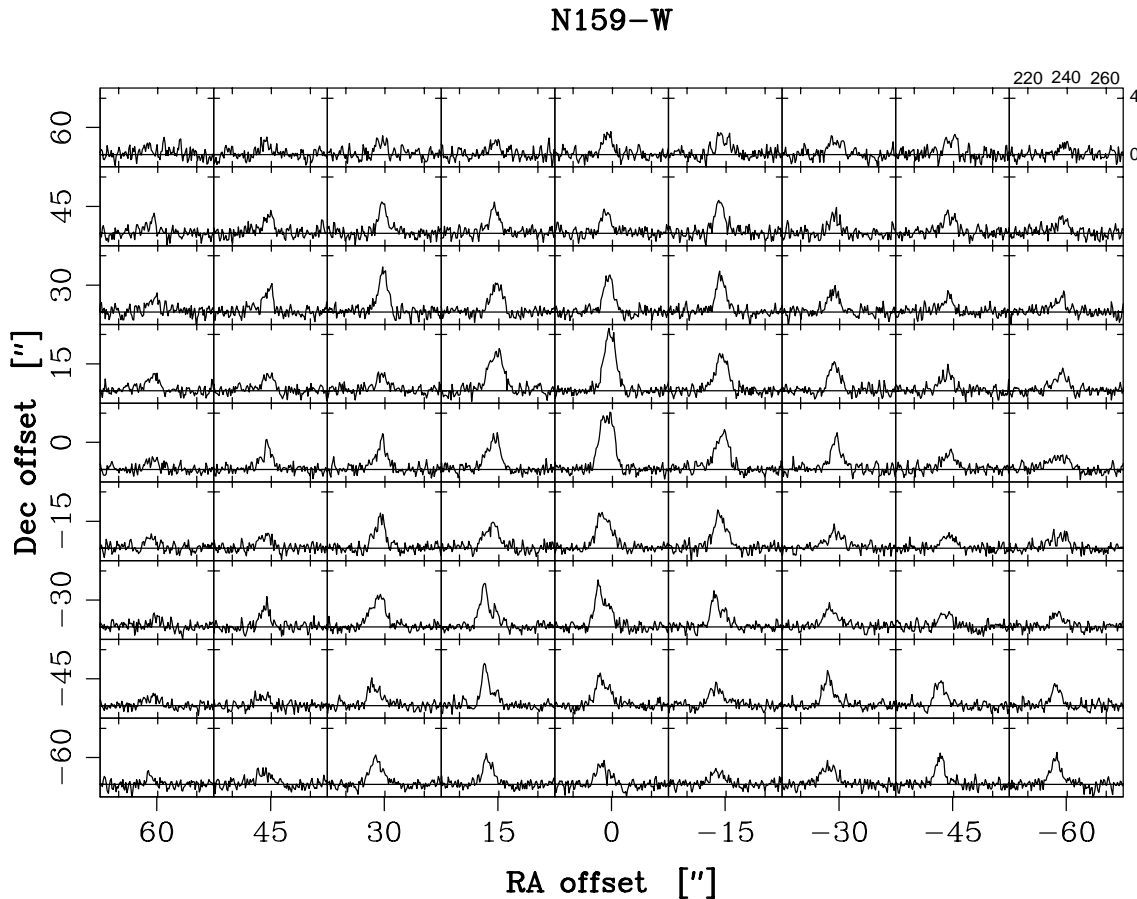
N159-W

Fig. 6. ^{12}CO(3–2) spectra observed towards the N 159 region (N159-W). Offsets are relative to $05^h40^m03^s.0$, $-69°47'03''$ (1950.0). The intensity scale is T_A^* [K] and velocities are given relative to lsr [km s^{-1}]. The velocity resolution is 0.5 km s^{-1}. The intensity and velocity scales are indicated in the upper righthand panel.

2.5 times larger. The latter clouds show smaller sizes, similar to the sizes observed in the LMC and SMC. When the conversion factors are plotted versus cloud sizes, the Galactic and Magellanic Clouds relations are largely indistinguishable (see Fig. 2 in Rubio (1997)).

Given the significantly different global properties of the Galaxy and of the Magellanic Clouds, and in particular of the SMC, the estimated conversion factors are surprisingly similar although the scatter is considerable – one order of magnitude (Rubio 1997). A significant part of the scatter is due to observational errors and uncertainties in the analysis. However, one would expect that clouds residing in the hostile environment of the 30 Dor nebula to have different conversion factors than clouds residing in more quiescent areas of the LMC. An important parameter in this context is the UV radiation which determines the molecular dissociation rates. Because CO is expected to be more sensitive to the UV flux than H$_2$, variations in the radiation field may have a strong effect on the conversion factor. From an analysis of far–infrared and HI data, Israel (1997) has recently presented estimates of the conversion factors for the Magellanic Clouds and other galaxies of similar types. The

analysis indicates that the conversion factor depends linearly on the ambient radiation field intensity per nucleon.

The two areas observed by us evidently show intrinsic differences with respect to the CO emission, emphasized by the non-LTE solutions presented above. To investigate possible variations of the conversion factor within the LMC, we show in Fig. 7 plots of CO luminosities, virial masses, and line widths, separately for the two fields. The scatter in the plots is, at least partly, observational (including errors that arise from the analysis). The observational uncertainties are dominated by the errors of the cloud size (note that the virial mass is proportional to the size). The relative errors of the size estimates increase with decreasing size, which follow from a combination of lower S/N ratios (weaker lines due to smaller beam-filling) and a higher weight of pointing errors when the beam–corrected sizes are estimated . Therefore, the slopes (in particular) of the least-squares fits shown in Fig. 7 suffer from relatively large uncertainties. In these plots the fits are determined by the (logarithmic) scatter in the size–dependent variables.

Similar to the conversion factor, one would expect a systematic difference in the degree of virial equilibrium between the violent region close to the 30 Dor nebula and the Southern
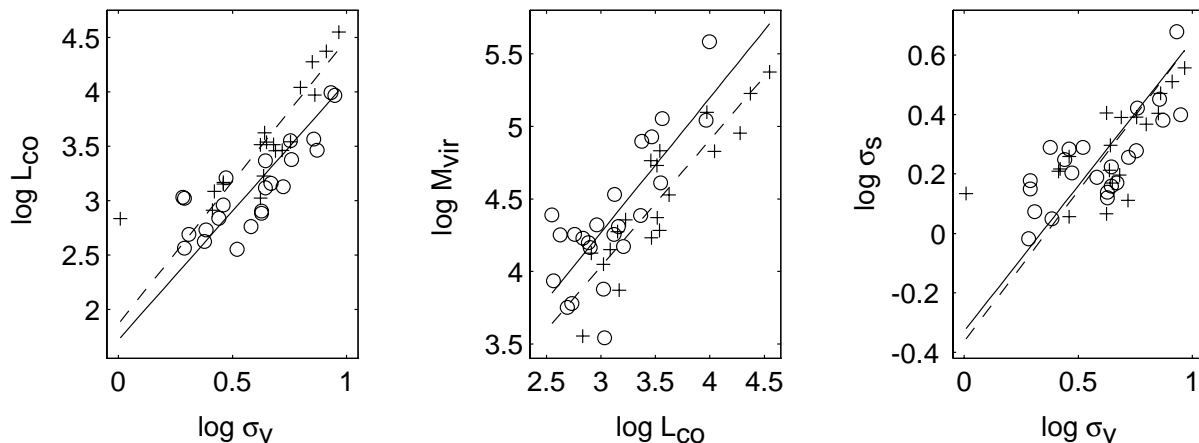
Fig. 7. a CO luminosity (K km s^{-1} pc^2) versus cloud size (pc), **b** virial mass (M$_\odot$) versus luminosity, and **c** size–line width dependence, for a sample of clouds in the 30 Doradus area (o) and the Southern field (+). The solid and dashed lines are least-squares fit regression lines.

area, conceivably revealed by higher velocity dispersions for clouds in the former area. However, the size–line width relations for the two fields are identical within the scatter, possibly indicating that any deviations in the other plots are unrelated to the size–line width dependence. The size–luminosity and luminosity–virial mass relations do show differences between the two fields, although small. Formally, clouds of the same size show CO luminosities higher by a factor of 2 in the Southern area. The same difference is indicated for clouds of similar virial masses. Provided that the virial mass is a good estimate of the H$_2$ mass, this difference translates to the same difference in the CO-H$_2$ conversion factor. The variation of the CO-H$_2$ conversion factor thus seems to be surprisingly small considering the very different physical environments (mainly the UV radiation fields). However, at the very best, the conversion factors determined in this way apply to that volume of the gas where the conditions for CO emission are favourable. This is based on the assumption that the virial–mass formula, with size and velocity dispersion defined by the CO emission, provides a measure of the mass within the CO boundary. Accordingly, any molecular gas outside the CO–emitting volume is presumably missed. In the Magellanic Clouds, the H$_2$ extents are expected to exceed those of CO in contrast to the situation for Galactic clouds (Maloney & Black 1988). In other words, the CO emission traces volumes of the clouds where the physical conditions suffer from less variations compared with the global cloud properties. This bias may partly explain the relatively small variations observed in the CO-luminosity/virial mass ratio. Another implication is that the derived CO-H$_2$ conversion factors underestimate the total H$_2$ contents in the Magellanic Clouds, particularly in the SMC (Maloney & Black 1988). On the other hand, these conversion factors may just provide upper limits to the H$_2$ content inside the CO emission regions if a significant fraction of the interclump hydrogen is atomic. This has been suggested to be the case for SMC clouds (Lequeux et al. 1994).

4.3. Comparison with other tracers

In order to understand the environment in which the molecular clouds reside, we list in Table 4 those objects which are detected in the line–of–sight and which may physically be associated with the clouds. The objects listed in this table are related to recent and current star formation. Unfortunately, the earlier radio–continuum and 21–cm observations have insufficient spatial resolution for detailed correlation studies; however, this situation may rapidly change with the operation of the Australian Interferometer. Besides the self–explanatory entries of Table 4, we make the following additional remarks:

Star clusters: The boundaries of the star clusters, or stellar associations, are difficult to define. The nuclear region of the stellar association N 2070 (LH 100) is the compact cluster R 136, recently investigated in detail with the HST by Hunter et al. (1996) and image–sharpening techniques by Brandl et al. (1996). The cluster R 136 dominates the radiation field, the ionization, and the dynamics of the 30 Doradus region. Although there are rich young stellar clusters in the southern H II regions (N 159: Deharveng & Caplan 1991, N 160: Heydari–Malayeri & Testor 1986), none of them has a core of similar brightness and compactness as R 136.

Extinction: The CO clouds and emission nebulae contain dust detectable as extinction and/or visible as dark nebulae. The entries in Table 4 give the global extinction A_V derived by Caplan & Deharveng (1985) from Hα/Hβ ratios measured through a diaphragm of 4$''$9 diameter. The low values of A_V indicate a low dust content in the observed areas, and in the LMC in general. However, the dust distribution is clumpy and locally the extinction may be 3 – 4 times higher than the global value.

Dark nebulae: Not all CO clouds observed are associated with dark nebulae as listed by Hodge (1972, 1988b), and vice versa. With respect to Lynds opacity classes 1 – 5 as used by Hodge, with class 5 identifying objects of the highest obscuration, the statistics of association with molecular clouds is given in Table 5. We find that $\sim 60\%$ and $\sim 75\%$ of the CO clouds in the 30 Dor area and the Southern field are associated with dark

Table 4. CO clouds and line–of–sight associated objects.

CO cloud [a]	Star Cluster [b]	A_V [c]	Dark Neb. [d]	IRAS [e]	Proto St. [f]	RS 6 cm [g]
30Dor–1				1472(C)		
30Dor–4,7,8			55 I	1384(4)		
30Dor–6	N2070, LH 100	1.4	87 I			MC 74
30Dor–5	N2070, LH 100	1.4	(99) II			MC 74
30Dor–10	N2070, LH 100	1.4	88 93 95 II		H1, H2, H4	MC 74
30Dor–12,13	N2070, LH 100	1.4	84 85 (88) II	1469(3120)	H3, H1	MC 74
30Dor–15	N2070, LH 100	1.4	84 85 II			MC 74
30Dor–11			60 I			
30Dor–20			56 104 II			
30Dor–17	N2060, LH 99	1.15	64 67 II			
30Dor–18	N2060, LH 99	1.15	76 II			
30Dor–22	N2060, LH 99	1.15	77 II	1448(312)		
30Dor–24			(72) II			
30Dor–27	N2044, LH 90	0.9	49 I	1383(220)		MC 69
30Dor–29,30			54 56 II	1429(104)		
30Dor–31,32			89 II	(1482(208))		
N158–1,3,5	N2074, LH 101	0.7	94 II 108 I	1490(312)		MC 75
N158–4,5			52 II	1485(C)		
N160–1,2,3	N2080, LH 103	0.8	114 I		E, J7	MC 76
N160–4,5	N2077, LH 103	0.8		1503(770)		
N160–6				(1549(C))		
N159–E	N20–78,83,84, LH 105	1.0	58 II	1518(624)	J28	MC 77
N159–W	N20–78,83,84, LH 105	1.0		1501(624)	G, J11	MC 77
N159–2	N2079, LH 105	1.0				
N159–5				(1523(C))		

a) Notation from Table 1.
b) Stellar clusters: Hodge & Wright (1967) [N], Lucke & Hodge (1970) [LH].
c) Global extinction (magnitude): Caplan & Deharveng (1985), derived from Hα/Hβ ratios.
d) Dark nebulae: Hodge (1972, 1988b), in brackets: doubtful. I: Lynds class $2-3$, II: Lynds class $4-5$.
e) IRAS sources: Schwering & Israel (1990), running number in list of IR sources (in brackets: 100–μm flux [Jy]).
f) Proto stellar objects: Hyland et al. (1992): H, Epchtein et al. (1984): E, Gatley et al. (1981): G,
Jones et al. (1986): J. The numbers indicate the objects in their corresponding tables.
g) Continuum radio sources at 6 cm: McGee et al. (1972).

Table 5. Association of Dark Nebulae (DN) and CO clouds.

Region	Opacity Class	DN associated with CO clouds	Total Number of DN
30 Dor	$5-4$	50 %	16
30 Dor	$3-2$	20 %	16
30 Dor	$5-2$	34 %	32
Southern Field	$5-2$	40 %	11

nebulae, respectively, and mostly with dark nebulae of opacity class $4-5$; we find that ~ 40 % of the dark nebulae are associated with CO clouds.

IRAS sources: The listed sources are IRAS point sources. For extended infrared emission measured by IRAS, see Schwering (1988), Schwering & Israel (1990), and Laspias & Meaburn (1991).

H I absorption: The measurements of Dickey et al. (1994) are made at 21 cm with the Australian interfero-meter against background continuum sources. These observations reveal for each background source several cold H I clouds in the LMC. Table 6 lists those H I clouds of which the systemic velocity is closest to the systemic velocity of the line–of–sight CO cloud.

The 21–cm observations give the H I column density as listed in Table 6. Dickey et al. state that the continuum source in the 30 Dor region is lying behind the LMC while the continuum sources of the Southern field are sources of the LMC, though probably located at the far side of the LMC.

OH and H_2O maser sources: There are two H_2O masers detected in our CO survey areas, 0539-691 and 0540-696 (Whiteoak & Gardner 1986). Nearby CO clouds are 30Dor-10 and N160-4, respectively. Towards the latter cloud, OH masers have been observed in the ground state at 1665 MHz and in an excited state at 6035 MHz (Caswell 1995).

Supernova remnants: There are two SNR in the 30 Dor area (see the compilation of Forest et al. 1988), i.e. SNR 0539–69.1 is associated in the line–of–sight with the CO cloud 30Dor–10, SNR 0538–69.1 is associated in the line–of–sight with the CO cloud 30Dor–22.

5. Summary

Using the Swedish–ESO Submillimetre Telescope (SEST), we have mapped the ^{12}CO(1–0) emission in the 30 Doradus region

Table 6. Line–of–sight association between CO clouds and H I clouds.

CO cloud	V [km s^{-1}]	ΔV [km s^{-1}]	$\log(L_{co})$ [K km s^{-1} pc^2]	H I cloud	V [km s^{-1}]	ΔV [km s^{-1}]	N_{HI} (10^{20}) [cm^2]	21–cm compon.
30Dor–29	247	4.2	3.13	0536–692	252	1.9	368	D
N159–E	238	6.0	4.28	0539–697	244	1.6	446	D
N159–W	234	7.6	4.37	0540–697	237	3.9	962	L
N160–4	237	4.7	3.62	0539–696	234	0.9	191	L

Column 1 – 4: from Table 1, column 5 – 8: from Dickey et al. (1994). The designation of the 21–cm velocity components D (disk) and L (characterized by lower velocities than in the disk) are from Luks & Rohlfs (1992).

in the Large Magellanic Cloud. Two fields were investigated: (i) one field including the 30 Doradus nebula (the "30 Dor" area), and (ii) an area, located some 30′ south of the former, which includes the H II regions N 158C, N 159 and N 160 (the "Southern" area). Each field was first mapped with a grid spacing of 40″ (30 Dor) and 60″ (Southern). Regions of significant CO emission were subsequently mapped with finer spacings of 20″ (30 Dor) and 20″ or 30″ (Southern). We also present CO(2–1) and CO(3–2) data for a sample of prominent CO clouds. Some results of CS(2–1) and HCO$^+$(1-0) observations are included as well.

Both fields show localized CO emission, "CO clouds", surrounded by large areas with relatively little or no CO gas. However, the surface filling factor of the CO emission is higher in the Southern area, at least on size-scales approaching the sizes of the investigated areas. Our non-LTE analysis of the CO emission in the three lowest rotational transitions indicates that this also applies to scales smaller than the CO(1–0) beam size (40″).

While the peak antenna temperatures in the ^{12}CO(1–0) transition are higher by a factor of 3 in the Southern area, the non-LTE analysis gives the highest kinetic temperature (about 50 K) towards the 30 Dor nebula. The higher kinetic temperature and lower filling factor of the CO emission in the central part of 30 Dor is most likely a result of the strong UV radiation field from the bright stellar cluster R 136.

We have separated the ^{12}CO(1–0) emission into 33 and 17 clouds in the 30 Dor and the Southern area, respectively. With a few exceptions, sizes, CO-luminosities, and virial masses are derived for this sample; the latter quantity is defined by CO parameters. Using the virial mass as an indicator of the total molecular mass, we have estimated the CO–H$_2$ conversion factor for the two areas separately. The size–line width relations are very similar in the two areas, while our data indicate a small difference in the CO luminosity/virial mass ratios. However, the difference is unexpectedly small in the light of the extreme physical conditions in the central parts of the 30 Dor area. We suggest that this is a bias effect in the sense that the CO emitting fraction of the cloud suffers from less variations of the physical conditions than the cloud as a whole. On the basis of previous theoretical work, we find it plausible that our conversion factor estimates only provide a lower limit to the total H$_2$ masses, and, possibly, an upper limit within the CO emitting volume.

Finally, we have collected data from the literature to identify possible associations between CO clouds, star formation tracers,

and dark nebulae. The most prominent CO clouds are associated with the formation of massive stars. A significant exception is the cloud N159-S. In the line–of–sight, about 60% of the CO clouds are associated with dark nebulae, as catalogued by Hodge (1972, 1988b), but only 40% of the nebulae with CO clouds.

Appendix A: derivation of cloud parameters

The basic cloud parameters have been determined assuming that the integrated emission can be described by a circular Gaussian distribution in the plane of sky. This allows a simple correction for the beam dilution when estimating emission extents: $s^2 = D^2 + B^2$, where D and B are the size of the cloud and the beam, respectively, and s is the observed emission extent.

The cloud parameters were determined by a numerical algorithm where the input parameters are the center velocities and widths of prominent line components in the investigated area. Only areas with a maximum grid–point spacing of 30″ (in most cases 20″) and a minimum number of 3 × 3 positions were investigated. Keeping the velocities and widths fixed, a simultaneous Gaussian fit of the amplitudes of all components were done at each position. Obviously, the derived amplitudes are sensitive to kinematic variations within the investigated area. However, the relevant variable in this context, the integrated emission, is more accurately determined provided that center velocity changes are relatively small (line–width changes have small effects). The four parameters of the circular distribution, i.e. peak intensity, peak position in α and δ, and emission extent, were then determined by fits to the integrated emission of each velocity component.

The assumption of a circular Gaussian distribution of the integrated emission may seem questionable when applying the virial mass formula to the derived parameters. Therefore, we have estimated the relevant corrections by testing the algorithm on a model cloud of ellipsoidal shape with different axial ratios (1–3), different extents relative to the beam (FWHM/major axis diameter = 0.3–3), and the two extreme cases of the optical depth of the emission. In the low–optical–depth limit, the emission is proportional to the column through the cloud. At high optical depths, the emission is constant inside the boundary of the cloud

and zero elsewhere. The equivalent radius of the cloud is defined as the harmonic mean of the major and minor axis radii.

As expected, the luminosity is well defined by the algorithm with, at most, a 10% correction within the parameter space above. This correction applies to an axial ratio of 1 and a source/beam size ratio of 3; for sources smaller than the beam, the corrections are at the 1% level.

The derived size corrections, here defined as the equivalent radius of the model cloud divided by the deconvolved size of the "observed" emission, show a larger spread: 0.65–0.85 and 0.7–0.95 for the low– and high–optical–depth cases, respectively. Thus, for the parameter space investigated, we find a factor of 0.8±20%. This is in good agreement with the empirical ratio for Galactic clouds found by Solomon et al. (1987). Applying this factor to the virial mass formula for a cloud with a r^{-1} volume density profile (MacLaren et al. 1988), we arrive at

$$M = 150 D \Delta v^2$$

where M is the total mass [$M_\odot$], D the FWHM of the integrated emission when modelled with a circular Gaussian distribution [pc], and Δv the FWHM of the observed line profile [km s^{-1}].

References

Baars J.W.M., 1973, IEEE Trans. Ant. Propagat. AP–21, 461

Bomans D.J., Points S., Weis K., et al., 1995, Rev. Mex. AA (Conf. Ser.) 3, 77

Booth R.S., 1993, New Aspects of Magellanic Cloud Research, B. Baschek, G. Klare, and J. Lequeux, eds., Springer, Berlin, p. 26

Brandl B., Sams B.J., Bertoldi F., et al., 1996, ApJ 466, 254

Caplan J., Deharveng L., 1985, A&AS 62, 63

Caswell J.L., 1995, MNRAS 272, L 31

Cheng K–P., Michalitsianos A.G., Hintzen P., et al., 1992, ApJ 395, L 29

Chin Y.-N., Henkel C., Whiteoak J.B., et al., 1997, A&A 317, 548

Chu Y–H., Kennicutt R.C., 1994, ApJ 425, 720

Cohen R.S., Dame T.M., Garay G., et al., 1988, ApJ 331, L 95

Cox P., Deharveng L., 1983, A&A 117, 265

Dall'Oglio G., Ade P.A.R., Andreani P., et al., 1995, A&A 303, 737

Deharveng L., Caplan J., 1991, A&A 259, 480

de Vaucouleurs G., Freeman K.C., 1972, Vistas in Astron. 14, 163

Dickey J.M., Mebold U., Marx M., et al., 1994, A&A 289, 357

Elliott K.H., Goudis C., Meaburn J., et al., 1977, A&A 55, 187

Elmegreen B.G., 1989, ApJ 338, 178

Epchtein N., Braz M.A., Sevre F., 1984, A&A 140, 67

Forest T.A., Spenny D.L., Johnson R.W., 1988, PASP 100, 683

Garay G., Rubio M., Ramirez S., et al., 1993, A&A 274, 743

Gatley I., Becklin E.E., Hyland A.R., et al., 1981, MNRAS 197, 17p

Graedel T.E., Langer W.D., Frerking M.A., 1982, ApJS 48, 321

Henize H., 1956, ApJS 2, 315

Heydari–Malayeri M., Testor G., 1986, A&A 162, 180

Hodge P.W., 1972, PASP 84, 365

Hodge P.W., 1988a, PASP 100, 1051

Hodge P.W., 1988b, PASP 100, 346

Hodge P.W., Wright F.W., 1967, The Large Magellanic Cloud Atlas, Smiths. Astrophys. Obs. Press

Hunter D.A., 1995, Rev. Mex. AA (Conf. Ser.) 3, 1

Hunter D.A., O'Neil E.J., Lynds R., et al., 1996, ApJ 459, L 27

Hyland A.R., Straw S., Jones T.J., et al., 1992, MNRAS 257, 391

Israel F.P. 1984, IAU Symp. 108: Structure and Evolution of the Magellanic Clouds, S. van den Bergh and K. S. de Boer, eds., Reidel, Dordrecht, p. 319

Israel F.P., 1997, A&A 328, 471

Israel F.P., de Graauw Th., 1991, IAU Symposium 148: The Magellanic Clouds, R Haynes and D. Milne, eds., Kluwer, Dordrecht, p. 45

Israel F.P., Koornneef J., 1991, A&A 250, 475

Israel F.P., de Graauw Th., van de Stadt H., et al., 1986, ApJ 303, 186

Israel F.P., Johansson L.E.B., Lequeux J., et al., 1993, A&A 276, 25 (Paper I)

Israel F.P., Maloney P.R., Geis N., et al., 1996, ApJ 465, 738

Issa M., MacLaren I., Wolfendale A.W., 1990, ApJ 352, 132

Jansen D., 1995, PhD Thesis, Leiden, The Netherlands

Johansson, L. E. B., 1991, IAU Symposium 146: Dynamics of Galaxies and Their Molecular Cloud Distribuition, F. Combes and F. Casoli, eds., Kluwer, Dordrecht, p. 1

Johansson L.E.B., Olofsson H., Hjalmarson A., et al., 1994, A&A 291, 89

Jones T.J., Hyland A.R., Straw S., et al., 1986, MNRAS 219, 603

Kutner M.L., Rubio M., Booth R.S., et al., 1997, A&AS 122, 255 (Paper VI)

Laspias V.N., Meaburn J., 1991, MNRAS 249, 1p

Lequeux J., Le Bourlot J., Pineau des Forets G., et al., 1994, A&A 292, 371

Lucke P.B., Hodge P.W., 1970, AJ 75, 171

Luks Th., Rohlfs K., 1992, A&A 263, 41

McGee R.X., Brooks J.W., Batchelor R.A., 1972, Aust. J of Phys. 25, 581

MacLaren I., Richardson K.M., Wolfendale A.W., 1988, ApJ 333, 821

Maloney P., 1990, ApJ 348, L 9

Maloney P., Black J.H., 1988, ApJ 325, 389

Mochizuki K., Nakagawa T., Doi Y., et al., 1994, ApJ 430, L 40

Norci L., Ögelman H., 1995, A&A 302, 879

Page T., Carruthers G.R., 1981, ApJ 248, 906

Parker J.W., Garmany C.D., 1993, AJ 106, 1471

Poglitsch A., Krabbe A., Madden S.C., et al., 1995, ApJ 454, 293

Rohlfs K., 1990, Tools of Radio Astronomy, Springer Verlag, p. 83

Rohlfs K., Kreitschmann J., Siegmann B.C., et al., 1984, A&A 137, 343

Rubio M., 1997, IAU Symposium 170: CO: Twenty-Five Years of Millimeter-wave Spectroscopy, W.B. Latter, S.J.E. Radford, P.R. Jewell, J.G. Mangum, and J. Bally, eds., Kluwer, Dordrecht, p. 265

Rubio M., Roth M., Garcia J., 1992, A&A 261, L 29

Rubio M., Lequeux J., Boulanger F., et al., 1993, A&A 271, 9

Schwering P.B.W., 1988, PhD Thesis, Leiden, The Netherlands

Schwering P.B.W., Israel F.P., 1990, Atlas and Catalogue of Infrared Sources in the Magellanic Clouds, Kluwer Academic Publisher, Dordrecht

Solomon P.M., Rivolo A.R., Barrett J.W., et al., 1987, ApJ 319, 730

Sternberg A., Dalgarno A., 1995, ApJS 99, 565

Strong A.W., Bloemen J.B.G.M., Dame T.M., et al., 1988, A&A 207, 1

van Dishoeck E.F., Black J.H., Phillips T.G., et al., 1991, ApJ 366, 141

Walborn N.R., Blades J.C., 1997, HST Preprint 1144

Wang Q.D., 1995, ApJ 453, 783

Wang Q., Helfand D.J., 1991, ApJ 370, 541

Whiteoak J.B., Gardner F.F., 1986, MNRAS 222, 513

Wilson C., 1995, ApJ 448, L 97

Westerlund B.E., 1990, A&A Rev. 2, 29